Supporting Information

Direct observation of cooperative protein structural dynamics of homodimeric hemoglobin from 100 picoseconds to 10 milliseconds with pump-probe X-ray solution scattering

Kyung Hwan Kim,[†,¶] Srinivasan Muniyappan,[†,¶] Key Young Oang,[†,¶] Jong Goo Kim,[†,¶] Shunsuke Nozawa,[‡] Tokushi Sato,[‡] Shin-ya Koshihara,[§] Robert Henning,[‖] Irina Kosheleva,[‖] Hosung Ki,[†] Youngmin Kim,[†] Tae Wu Kim,[†] Jeongho Kim,[†] Shin-ichi Adachi,[‡,°] Hyotcherl Ihee*,[†]

[†] Center for Time-Resolved Diffraction, Department of Chemistry, Graduate School of Nanoscience & Technology (WCU), KAIST, Daejeon, 305-701, Republic of Korea

[‡] Photon Factory, Institute of Materials Structure Science, High Energy Accelerator Research Organization (KEK), 1-1 Oho, Tsukuba, Ibaraki 305-0801, Japan

[§] Department of Chemistry and Materials Science, Tokyo Institute of Technology and CREST, Japan Science and Technology Agency (JST), Meguro-ku, Tokyo 152-8551, Japan

[‖] Center for Advanced Radiation Sources, The University of Chicago, Chicago, IL 60637, USA

[°] PRESTO, Japan Science and Technology Agency (JST), 4-1-8 Honcho, Kawaguchi, Saitama 332-0012, Japan

[¶]These authors equally contributed to this work.

*Corresponding authors: hyotcherl.ihee@kaist.ac.kr

Sample preparation

The HbI was over-expressed in *Escherichia coli* and purified as described previously [1]. The F97Y mutation was introduced into the native recombinant HbI gene using the EZchange® mutagenesis kit (Enzynomics™) with the following primers encoding F97Y mutation: 5'-TGTTGTTGAAAAATATGCTGTTAACCA-3' and 5'-ATGGTTAACAGCATATTTTTCAA CAACA-3' (Genotech). The F97Y mutant was over-expressed and purified as described for wild type. Carbonmonoxy dimeric hemoglobin ($HbI(CO)_2$) solution was prepared as follows. A 2 – 4 mM HbI solution in 100 mM phosphate buffer (pH 7) was prepared in a rubber-topped air-tight vial. The concentration of the protein was determined from the absorbance at 578 nm using the absorption coefficient of heme-oxygenated derivatives (14.3 mM^{-1} cm^{-1}). The HbI was reduced by adding 10 μL of 1 M sodium dithionite solution to the HbI solutions under nitrogen atmosphere. The reduced samples were exposed to CO gas for 30 minutes to convert HbI to the CO-bound HbI ($HbI(CO)_2$). The sample solutions were prepared just before the X-ray solution scattering measurement. An aliquot of the resulting $HbI(CO)_2$ solution was transferred into a 1-mm diameter X-ray capillary (Hampton Research) and immediately sealed with epoxy to minimize gas exchange while CO gas was purged continuously into the capillary.

Data collection

Time-resolved X-ray solution scattering data were collected both at the 14IDB BioCARS beamline at the Advanced Photon Source and NW14A beamline at the KEK. Summary of beamtimes used for the data collection is summarized in Table S1.

(1) Data collection at APS

Standard operating top-up mode of the Advanced Photon Source was used for early delays (from 100 ps to 562 ns) and 324 bunch mode was used for late delays (from 562 ns to 56.2 ms), The X-ray spectrum is peaked at 12 keV with a long wavelength tail and the bandwidth is ~4 % FWHM. To reduce the data acquisition time, the full spectrum was used without being monochromatized. The blurring effect to the scattering curve due to the polychromaticity with the ~4% bandwidth is not substantial. The 100-ps-long (FWHM) X-ray pulse containing ~10^9 photons was focused by Kirkpatrick-Baez focusing mirrors, trimmed by slits and delivered to the

sample position at a spot size of 0.1 × 0.07 mm^2 (horizontal × vertical, FWHM). Single X-ray pulses were isolated from the high-frequency pulse train by a heat-load chopper, a Jülich high-speed chopper and a millisecond shutter. The heat-load chopper positioned upstream of the high-speed chopper and the shutter reduces the heat load to the high-speed chopper. Single X-ray pulses are isolated by the high-speed chopper that has a triangular-shaped rotor with a tunnel spinning at ~1 kHz, a subharmonic of the synchrotron. The repetition rate was further reduced from 1 kHz down to 40 Hz or 10 Hz using a millisecond shutter to allow long time delays and enough time to move the probing spot to a fresh position at every pair of laser and X-ray pulses. The protein sample was excited by ~35-ps laser pulses at 532 nm generated by the picosecond laser system at the 14IDB beamline. Femtosecond pulse train at 780 nm were generated from a Tsunami Ti:sapphire laser oscillator and was used to seed the picosecond amplifier system (Spectra Physics Spitfire Pro). The output from the amplifier was sent to a TOPAS optical parametric amplifier to convert the wavelength to 532 nm and was stretched to ~35 ps by an echelon stretcher. The laser pulse of ~68 μJ energy was focused to a spot of 0.125 × 0.60 mm^2 size at the sample position. Power density of the laser was controlled by a variable ND filter, yielding the fluence of 0.25 (low), 0.5 (mid), or 1.0 (high) $\mu J/mm^2$. The sample was contained in a sealed capillary with 1-mm diameter and excited by a laser pulse from the top. The sample temperature was maintained at 25 °C with a cold nitrogen stream (Oxford Cryostream). The X-ray pulse probes 0.2 mm deep from the top in perpendicular geometry. The X-ray pulses scattered by the sample were collected with a two-dimensional MarCCD. To reduce the background scattering from the air, a cone filled with helium gas was used between the sample and the MarCCD. To avoid the radiation damage and provide fresh sample for each pair of X-ray and laser pulses, the capillary containing the sample was translated back and forth along its long axis over a 20-mm range with the movement synchronized with the pulse trains of laser and X-rays.

The laser-off images were acquired with the laser pulse arriving 5 μs later than the X-ray pulse in order to probe the (unexcited) ground state while assuring the same average temperature of the sample solution. These laser-off images were used as a reference for calculating the time-resolved difference X-ray scattering patterns. Usually, a laser-off image was collected after every

3 or 4 laser-on images to compensate for slow drifts of the X-ray intensity in the beamline. To attain enough signal-to-noise ratio, about 20 images were acquired at each time delay. The measured time delays are basically spread evenly in logarithmic time scale as follows: –5 μs, 108 ps, 167 ps, 246 ps, 352 ps, 492 ps, 680 ps, 930 ps, 1.26 ns, 1.71 ns, 2.30 ns, 3.09 ns, 4.15 ns, 5.55 ns, 7.43 ns, 10 ns, 13.3 ns, 17.8 ns, 23.7 ns, 31.6 ns, 42.2 ns, 56.2 ns, 75 ns, 100ns, 133 ns, 178 ns, 237 ns, 316 ns, 422 ns, 562 ns, 750 ns, 1 μs, 1.33 μs, 1.78 μs, 2.37 μs, 3.16 μs, 4.22 μs, 5.62 μs, 7.5 μs, 10 μs, 13.3 μs, 17.8 μs, 23.7 μs, 31.6 μs, 42.2 μs, 56.2 μs, 75 μs, 100 μs, 133 μs, 178 μs, 237 μs, 316 μs, 422 μs, 562 μs, 750 μs, 1 ms, 1.33 ms, 1.78 ms, 2.37 ms, 3.16 ms, 4.22 ms, 5.62 ms, 7.5 ms, 10 ms, 13.3 ms, 17.8 ms, 23.7 ms, 31.6 ms, 42.2 ms, 56.2 ms. To reduce the data collection time, the data collection was divided into three parts. For time delays shorter than 562 ns, 100-ps single X-ray pulses were used, for time delays between 562 ns and 5.62 μs, 250-ns pulses from the 324 bunch mode were used, and for the time delays larger than 5.62 μs, a 1.5-μs pulse train containing multiple X-ray pulses was used. Details of the data collection parameters are summarized in Table S2. The 31.6 μs time delay was used as a common time point for comparison between the data sets from different measurements, that is, we checked if the 31.6 μs data from different measurements were identical within the signal-to-noise ratio (see Figure S1).

(2) Data collection at KEK

Single-bunch mode of the Photon Factory Advanced Ring of KEK was used. A capillary containing $HbI(CO)_2$ solution was mounted in a goniometer so that its axis is perpendicular to the directions of the laser and X-ray pules, which are also perpendicular to each other. To initiate a photoreaction, we used two types of laser pulses at NW14A: picosecond and nanosecond laser pulses at 527 nm. The 120-fs, 800 nm laser pulses from a femtosecond amplified laser system (Spectra-Physics) were converted to femtosecond laser pulses centered at 527 nm by TOPAS, and then stretched to ~10 ps duration by a stretcher using a pair of reflective gratings. The nanosecond laser pulses of 8 ns pulse duration were generated from a solid-sate nanosecond laser (Continuum Powerlite8000) utilizing an OPO setup (Continuum PantherOPO) pumped by the third harmonic of a Nd:YAG laser. The laser beam was sent down to the sample vertically and

was focused to an elliptical spot at the top part of the capillary. The energy density was 0.7 – 2.3 mJ/mm^2 and 0.5 mJ/mm^2 for the ns and ps excitations, respectively. The X-ray pulses were generated by passing the electron bunches through two undulators with 20 and 36 mm periods. Since the bandwidth of the X-ray pulses generated from the undulators is too broad ($\Delta E/E >$ 15%), we used a multilayer optic that is made of depth-graded Ru/C layer (average d = 40 Å, NTT Advanced Technology), was used to reduce the bandwidth down to 5% with the X-ray peak centered at 15.7 keV (0.79 Å). When the multilayer optic with 5% energy bandwidth is used downstream the Jülich chopper, the photon flux of 3×10^8 photons/pulse is obtained. The blurring effect to the scattering curve due to the polychromaticity is not substantial with the ~5% bandwidth.

The 120-ps (FWHM) X-ray pulses were focused by bent-cylindrical focusing mirrors, trimmed by slits and delivered to the sample with a focal spot size of 0.44×0.11 mm^2 (horizontal × vertical, FWHM). Single X-ray pulses were isolated from the high-frequency pulse train by a heat-load chopper, a Jülich high-speed chopper and a millisecond shutter. The heat-load chopper positioned upstream of the rest reduces the heat load to the high-speed chopper. Single X-ray pulses are isolated by the high-speed chopper where a triangular-shaped rotor with a tunnel is spinning at ~1 kHz, a subharmonic of the synchrotron. The repetition rate was further reduced from 1 kHz down to 10 Hz using a millisecond shutter to allow the measurement at long time delays and enough time to move the probing spot to a fresh position at every scattering image.

The X-ray pulse passes through the capillary at the position of 0.3 mm from the top in the perpendicular geometry to the capillary. The X-ray pulses scattered by the sample were collected with a two-dimensional MarCCD detector. To reduce the scattering from the air, a chamber filled with helium gas was used between the sample and the detector. The laser-off images were acquired with the laser pulse arriving 5 μs later than the X-ray pulse in order to probe the ground state while assuring the same average temperature of the solution. These laser-off images were used as a reference for calculating the time-resolved difference X-ray scattering patterns. Usually, a laser-off image was collected after every 3 or 4 laser-on images to compensate for slow drifts in the beamline. To attain enough signal-to-noise ratio, about 30 – 70 images were acquired at

each time delay. The measured time delays are basically spread evenly in logarithmic time scale as follows. The time delays for ps excitation are –5 μs, 100 ps, 178 ps, 316 ps, 562 ps, 1 ns, 1.78 ns, 3.16 ns, 5.62 ns, 10 ns, 30 μs, and 30 ms. The time delays for ns excitation are –5 μs, 10 ns, 30 ns, 100 ns, 178 ns, 300 ns, 562 ns, 800 ns, 1 μs, 1.78 μs, 3 μs, 5.62 μs, 8 μs, 10 μs, 30 μs, 56.2 μs, 100 μs, 178 μs, 300 μs, 562 μs, 1 ms, 1.78 ms, 3 ms, 4 ms, 5.62 ms, 8 ms, 10 ms, 17.8 ms, 30 ms, and 56.2 ms. To reduce the data collection time, the data collection was divided to two parts. For time delays shorter than 30 μs, 120-ps single X-ray pulses were used, but for the time delays larger than 30 μs, a 11-μs pulse train containing 10 X-ray pulses separated by 1.26 μs was used.

Data processing

Two-dimensional scattering images were azimuthally averaged to give one-dimensional scattering curves. To convert the scattering angle (θ) to q, the center-of-mass position of the undulator spectrum was used as the reference wavelength. The laser-induced scattering intensity changes are less than a few percent of the static scattering intensity and thus a careful normalization is necessary to extract accurate laser-induced scattering differences. As a normalization reference, we used the q position of 2.07 $Å^{-1}$, which is the isosbestic point of the water scattering curves with respect to temperature increase, so that the difference scattering intensity at this q value is zero. In Figure S2, the data at 31.6 ms is presented as an example. At this time delay, the signal at low q values is negligible, indicating the absence of the contribution from transiently generated species. Moreover, the difference curve at 31.6 ms can be well represented by a sum of scattering intensity changes from bulk water arising from the temperature change at constant density ($(\partial S(q)/\partial T)_\rho$) and the density change at constant temperature ($(\partial S(q)/\partial \rho)_T$) as shown in Figure S2, confirming that the difference scattering at late time delays are mainly attributed to solvent heating. To remove the solvent heating effect, this signal from solvent heating was subtracted from the difference curves at all time delays (see Figure S3 and Figure S4)

Data analysis

(1) Singular value decomposition

In order to determine the kinetic model, we need to examine how many distinct transient species are involved in the dynamic process of interest and how fast the population of each species changes after photolysis. For this purpose, we applied the singular value decomposition (SVD) analysis and kinetic analysis, which will be detailed in the next section, to our experimental data in the q-range of 0.15 – 1.0 Å^{-1}. From the experimental scattering curves measured at various time delays, we can build a $n_q \times n_t$ matrix $\mathbf{A}$, where n_q is the number of q points in the scattering curve at a given time-delay point and n_t is the number of time-delay points. For the data presented in this paper, n_q and n_t are 416 and 69, respectively. Then, the matrix $\mathbf{A}$ can be decomposed while satisfying the relationship of $\mathbf{A}=\mathbf{USV}^{\mathrm{T}}$, where $\mathbf{U}$ is an $n_q \times n_t$ matrix whose columns are called left singular vectors (i.e. time-independent q spectra) of $\mathbf{A}$, $\mathbf{V}$ is an $n_t \times n_t$ matrix whose columns are called right singular vectors (i.e. amplitude changes of $\mathbf{U}$ as time evolves) of $\mathbf{A}$, and $\mathbf{S}$ is a diagonal $n_t \times n_t$ matrix whose diagonal elements are called singular values of $\mathbf{A}$ and can possess only non-negative values. The matrices $\mathbf{U}$ and $\mathbf{V}$ have the properties of $\mathbf{U}^{\mathrm{T}}\mathbf{U}=\mathbf{I}_{n_t}$ and $\mathbf{V}^{\mathrm{T}}\mathbf{V}=\mathbf{I}_{n_t}$, respectively, where $\mathbf{I}_{n_t}$ is the identity matrix. Since the diagonal elements (i.e. singular values) of $\mathbf{S}$, which represent the weight of left singular vectors in $\mathbf{U}$, are ordered so that $s_1 \geq s_2 \geq \ldots \geq s_n \geq 0$, (both left and right) singular vectors on more left are supposed to have larger contributions to the constructed experimental data. In this manner, we can extract the time-independent scattering intensity components from the left singular vectors and the time evolution of their amplitudes from the right singular vectors. The former, when combined together, can give the information on the scattering curves of distinct transient species, while the latter contains the information on the population dynamics of the transient species. Thus, the SVD analysis provides a model-independent estimation of the number of structurally distinguishable species and the dynamics of each species.

As shown in Figure S5 and Figure S6, the singular values and autocorrelation values of the corresponding singular vectors suggest that three singular vectors are enough to represent our

experimental data of HbI. In other words, the contribution from the fourth singular vector and beyond becomes negligible. In this regard, the first three right singular vectors multiplied by singular values were fit by seven exponentials sharing common relaxation times, yielding the relaxation times of 3.2 (± 0.2) ns, 93 (± 20) ns, 730 (± 120) ns, 5.6 (± 0.8) μs, 15.2 (± 8) μs, 1.8 (± 0.3) ms, and 9.1 (± 0.9) ms, for wild-type HbI excited with 'mid' laser fluence (measured at APS) (see Figure S5). The same fitting procedure was performed for F97Y mutant HbI excited with 'mid' laser fluence (measured at APS), and the relaxation times of 3.0 (± 0.3) ns, 40 (± 20) ns, 370 (± 100) ns, 4.7 (± 3.1) μs, 25.9 (± 13.8) μs, and 330 (± 40) μs were obtained (see Figure S6).

(2) Kinetic analysis

Using the first three singular vectors of significant singular values obtained from the SVD analysis, we performed kinetic analysis. New matrices, $\mathbf{U}'$, $\mathbf{V}'$ and $\mathbf{S}'$, can be defined by removing non-significant components from $\mathbf{U}$, $\mathbf{V}$ and $\mathbf{S}$, respectively. In other words, $\mathbf{U}'$ is an $n_q \times 3$ matrix containing only the first three left singular vectors of $\mathbf{U}$, $\mathbf{S}'$ is a 3×3 diagonal matrix containing the first three singular values of $\mathbf{S}$, and $\mathbf{V}'$ is an $n_t \times 3$ matrix containing the first three right singular vectors of $\mathbf{V}$. Here we represent the time-dependent concentrations of transiently formed intermediate species, which can be calculated from a kinetic model, by a matrix $\mathbf{C}$. Then, the matrix $\mathbf{C}$ can be related to $\mathbf{V}'$ by using a parameter matrix $\mathbf{P}$ that satisfies $\mathbf{V}' = \mathbf{CP}$. In our analysis, $\mathbf{C}$ is an $n_t \times 3$ matrix containing the time-dependent concentrations of three intermediates of HbI, that is, the earliest I_1 intermediate, the early R-like I_2 intermediate and the late T-like I_3 states, and $\mathbf{P}$ is a 3×3 matrix containing coefficients for the time-dependent concentrations so that the linear combination of concentrations of the three intermediates can form the three right singular vectors in $\mathbf{V}'$. Once $\mathbf{C}$ is specified by a kinetic model with a certain set of variable kinetic parameters such as rate coefficients, $\mathbf{P}$ and $\mathbf{C}$ can be optimized by minimizing the discrepancy between $\mathbf{V}'$ and $\mathbf{CP}$.

However, standard deviations for $\mathbf{V}'$ are not available from the experimental data and thus we instead used the following method to optimize $\mathbf{P}$ and $\mathbf{C}$. Since $\mathbf{V}' = \mathbf{CP}$, the following relationships hold.

$$\mathbf{A'} = \mathbf{U'S'V'}^{\mathrm{T}} = \mathbf{U'S'(CP)}^{\mathrm{T}} = \mathbf{U'S'(P}^{\mathrm{T}}\mathbf{C}^{\mathrm{T}}) = (\mathbf{U'S'P}^{\mathrm{T}})\mathbf{C}^{\mathrm{T}} \quad (1)$$

where $\mathbf{A'}$ is an $n_q \times n_t$ matrix that contains the theoretical difference scattering curve $\Delta S_{theory}(q_i, t_j)$ at given q and t values. Theoretical difference scattering curves calculated by using Eqn. (1) were compared with the experimental difference scattering curves, and the matrices **P** and **C** were optimized by minimizing the discrepancy χ_i^2 between the theoretical and experimental difference scattering curves using the Minuit package:

$$\chi_i^2 = \sum_{j=1}^{n_t} \left(\frac{\Delta S_{\exp}(q_i, t_j) - \Delta S_{\text{theory}}(q_i, t_j)}{\sigma_{ij}} \right)^2 \quad (2)$$

where $\Delta S_{\exp}(q_i, t_j)$ and $\Delta S_{\text{theory}}(q_i, t_j)$ are the experimental and theoretical difference scattering curve at given q and t values, respectively, and σ_{ij} is the experimental standard deviation at given q and t values. From Eqn. (1), we can define a matrix $\mathbf{B}$ as $\mathbf{B} = \mathbf{U'S'P}^{\mathrm{T}}$, that is, a linear combination of the three left singular vectors in $\mathbf{U'}$ weighted by their singular values in **S'** with their ratios determined by **P**. Then, the matrix $\mathbf{B}$, an $n_q \times 3$ matrix, contains the three difference scattering curves directly associated with the three intermediate species of HbI (shown in Figure 3B). Therefore, by optimizing the matrices **P** and **C**, we obtain both the time-dependent concentrations (optimized **C**; see Figure S5D and Figure S6D) and the (time-independent) scattering curves of the intermediate species (optimized $\mathbf{B}$).

(3) The kinetic model

To analyze the kinetics of both wild type and F97Y mutant, we used a kinetic model involving biphasic kinetics, geminate recombination, and bimolecular CO recombination, as described in Figure 3A. Based on the results of the SVD analysis, where the first three singular values were determined to be dominantly large, we considered three intermediates (I_1, I_2 and I_3). Each intermediate species can have both fully photolyzed and partially photolyzed forms. The red (with "CO") and white symbols in Figure 3A indicate the liganded and photolyzed subunits, respectively. Based on our structural analysis, the subunits of each intermediate are represented with different shapes of symbols to indicate the change in the tertiary structure. In the I_3 intermediate, one subunit is described to rotate versus the other, reflecting the quaternary

structural change in the transition from I_2 to I_3. The relaxation times obtained from fitting the first three right singular vectors multiplied by singular values with a sum of exponentials were used as time constants describing the kinetic model. The I_1 intermediate transforms to the I_2 intermediate with a time constant common for both fully photolyzed and singly photolyzed forms (3.2 ns for wild type and 3.0 ns for F97Y). A portion of the I_2 intermediates geminately recombine with CO to return to the non-photolyzed form of the I_1 intermediate with a time constant of 93 ns (for both wild type and F97Y). which then ultimately decays to the initial $HbI(CO)_2$ structure (15.2 μs for wild type and 4.7 μs for F97Y). Subsequently, the I_2 intermediate is converted to the I_3 intermediate with ligation-dependent, biphasic dynamics. The ground state $HbI(CO)_2$ is recovered via two different pathways: (1) bimolecular (non-geminate) CO recombination from I_3 and (2) geminate recombination from I_2 through a non-photolyzed form of I_1. Using this kinetic model, we optimized (1) the ratio of geminate and non-geminate recombination, (2) the ratio between fully and partially photolyzed forms, (3) the rate for non-geminate recombination, and (4) the matrix **P** so that the theoretical scattering curves (obtained from linear combinations of species-associated scattering curves) well matches the experimental, time-dependent difference scattering curves for all the data sets measured at three different laser fluence levels. The theoretical scattering curves fit into the experimental curves for the wild type and F97Y mutant at the mid laser fluence are shown in Figure S7 and Figure S8, respectively. Definitions for parameters in the kinetic model are listed in Table S3. Fitting parameters obtained from the kinetic analysis of the data measured at APS and KEK are summarized in Table S4 and Table S5, respectively. For F97Y, the SVD analysis does not show the 93-ns component which is clearly observed in the wild type data and is assigned to geminate combination from I_2 to a non-photolyzed form of I_1. Nevertheless we included the 93-ns component because the kinetic component (4.7 μs) corresponding to the recovery of $HbI(CO)_2$ from a non-photolyzed form of I_1 is still observed for F97Y. As a matter of fact, the portion of geminate recombination is almost negligible compared with wild type and a satisfactory fit can be obtained even without including the recovery of $HbI(CO)_2$ via geminate recombination.

(4) Calculation of theoretical x-ray scattering curves

To calculate the solution scattering curves from given protein structures generated by the simulation, we used CRYSOL version 2.6 [2]. In the calculation performed by this program, three components are considered: (1) scattering of atoms in vacuo $A_a(\mathbf{q})$, (2) scattering from the excluded volume $\rho_s A_s(\mathbf{q})$, and (3) scattering from hydration shell $\delta\rho_b A_b(\mathbf{q})$. The scattering intensity is calculated by the following equation:

$$S(q) = < \left| A_a(\mathbf{q}) - \rho_s A_s(\mathbf{q}) + \delta\rho_b A_b(\mathbf{q}) \right|^2 >_\Omega \quad (3)$$

where ρ_s is the electron density of the bulk solvent and $\delta\rho_b = (\rho_b - \rho_s)$ is the contrast between the hydration shell and bulk solvent where ρ_b is the electron density of the hydration shell.

To take into account the effect of polychromatic X-ray used in the experiment, a "polychromatic correction" was applied to the scattering curves calculated from CRYSOL. The scattering curves calculated with monochromatic X-ray at a single X-ray wavelength are regenerated at various wavelengths in the X-ray wavelength distribution. Then, by taking the weighted sums of the regenerated curves in proportion the photon flux at each wavelength in the X-ray spectrum, polychromatic-corrected scattering curves are obtained.

The version of CRYSOL (version 2.6) we employed is designed for scattering calculation at wide angles up to 1 $Å^{-1}$ by employing higher number of harmonics to account for the scattering at the wide angles. We also compared the CRYSOL calculation with a calculation using FoXS program[3], which makes use of Debye formula instead of multipole expansion used in CRYSOL. As shown in Figure S9, the results of the two calculations are in good agreement.

(5) Structure refinement aided by Monte Carlo simulations of rigid-body movement

To obtain more detailed structural insight to the tertiary and quaternary structural changes of HbI, we developed a structure refinement procedure aided by Monte Carlo (MC) simulations using the species-associated difference curves obtained from the kinetic analysis. In the rigid-body modeling, the whole protein structure is divided into a number of rigid bodies and the rigid bodies are allowed to move under the influence of a certain set of force fields until a certain criterion is met against the experimental data. The basic assumption in the rigid-body modeling is that the short-range structural parameters of the solution structure are similar to those of

already available crystallographic structures. This means that we can reduce the number of variable parameters by grouping many nearby atoms (for example those in a helix) into a rigid body in which bond lengths and bond angles are fixed at the same values as those of crystallographic structures. In a sense, this approach is similar to molecular replacement in X-ray crystallography. In our case, each subunit of the HbI intermediate is divided into nine rigid bodies, that is, eight helices and one heme group, resulting in a total of eighteen rigid bodies in the entire HbI protein.

To avoid being trapped in local energy minima, we generated many starting structures for the structure refinement, instead of using only one crystal structure, by randomly moving the rigid bodies of known crystal structures of HbI using the MC simulation. For example, the crystal structure formed at 5 ns after the photolysis of carbonyl ligands (PDB code: 2grz) was modified to generate starting structures of the I_1 and I_2 intermediates, while the deoxy crystal structure (PDB code: 4sdh) was used for the I_3 (WT) and I_3 (F97Y) (where Phe97 residue in each unit of 4sdh were replaced by Tyr97 residues in the F97Y mutant) intermediates. The carbonmonoxy crystal structure (PDB code: 3sdh) was used for CO-bound HbI in solution, and the scattering curve of 3sdh was subtracted from the scattering curves of the wild-type intermediate structures to calculate the difference scattering curves of the intermediates. For I_3 (F97Y), the carbonmonoxy F97Y crystal structure (PDB code: 2auo) was used for CO-bound F97Y HbI in solution and the scattering curve of 2auo was subtracted in the same manner as for the wild type.

When generating random structures using the MC simulation, a constraint was applied to maintain the symmetry between two subunits of HbI. To do so, randomly reorganized rigid bodies of one subunit were duplicated in the other subunit via translation and rotation operations so that the tertiary structures of both subunits are identical. As a result, hundreds of random structures with symmetric subunits were generated within RMSD (root-mean square deviation) of 1.2 Å, which is twice as large as the RMSD between carbonmonoxy- and deoxy- HbI crystal structures (0.6 Å).

In the structure refinement, we included an additional strategy to alleviate the problem of trapping in local energy barriers. Once it appears that the current structure is trapped in a minimum (either global or local), that structure is given a chance to escape from that minimum

by applying relatively large chi-square force as a perturbation while other forces being maintained the same. Then, the structure is refined again after this perturbation. If the structure still cannot overcome the trap despite the perturbation, the final structure of this run is recorded and a new independent simulation is started with another random structure that has not been used. This step continues until all hundreds of random structures are examined.

The goal of the structure refinement is to find a structure that minimizes the target function value. The target function, E, contains E_{data} to represent the difference between experimental curve and theoretical curve and E_{chem} to represent the penalty proportional to the chemical interactions of the non-bonded short-range repulsion and symmetry restraints between two subunits.

$$E = E_{data} + E_{chem} \tag{4}$$

The E_{data} term is represented by chi-square value between a theoretical curve from the simulation and a time-independent species-associated curve as follows:

$$E_{data} = w_1 \sum_{q=1}^{N_q} \left(\frac{\Delta S_{\exp}(q) - c_s \Delta S_{cal}(q)}{\sigma_q} \right)^2 \tag{5}$$

where c_s is the scaling factor between theoretical difference curves from the simulation and experimental difference curves and the w_2 is the weighting factor for the E_{data} term.

The E_{chem} term contains the components of collision and symmetry restraints as follows.

$$E_{chem} = w_2 \sum_{\substack{nonbonded \\ contact}} 4\left(\frac{\sigma^{12}}{r_{ij}^{12}} - \frac{\sigma^{6}}{r_{ij}^{6}} \right) + w_3 \left\{ \sum_{i=1}^{2/N} \sum_{j=1 \neq i}^{2/N} \left(r_{ij} - r_{i+\frac{N}{2}, j+\frac{N}{2}} \right)^2 + \sum_{i=\frac{N}{2}+1}^{N} \sum_{j=\frac{N}{2}+1 \neq i}^{N} \left(r_{ij} - r_{i-\frac{N}{2}, j-\frac{N}{2}} \right)^2 \right\} \tag{6}$$

where N means the total number of atoms in the protein. The first term in E_{chem} is the Lennard-Jones potential to give penalty to collision of atoms. The second term in E_{chem} gives penalty to the difference in distances between the same combinations of two atoms in both subunits, which restrains that the two subunits share as similar tertiary structure as possible. The w_2 and w_3 are the weighting factors for the two terms. Determination of appropriate weighting factors w_1 to balance the magnitude of two terms, E_{data} and E_{chem}, is important. If w_1 is too large, the refined structure may have an unphysical geometry. In contrast, if w_1 is too small, the refined structure may not satisfy the experimental data.

The rigid bodies are moved randomly until the lowest target function value can be found, but this approach is rather slow in minimizing the target function value. To speed up the convergence, in our approach, the movements of the rigid bodies are determined according to the three potential terms with the total potential (U_{tot}) represented as follows.

$$U_{tot} = c_1 U_{LJ} + c_2 \chi^2 + c_3 U_{SS} \quad (7)$$

where U_{LJ}, χ^2 and U_{SS} are the chemical, chi-square, and symmetry force fields, respectively, and c_1, c_2 and c_3 are weighting factors to scale the magnitude of three terms. Since the atomic structure within a rigid body is constrained to be the same as that of the crystal structure, the force field within the rigid body is not needed, and only the Van der Waals interactions (U_{LJ}) between rigid bodies are included in the chemical force field. The chi-square potential (χ^2) represented by χ^2 value between theoretical curve generated from the simulation and time-independent species-associate curves from the experiment drives the structure generated by simulations toward a structure that fits the experimental curve [4-5]. The structural symmetry term (U_{SS}) is used to restrain the symmetry of two subunits. The movements of rigid bodies are governed by these three force fields. Eq. (7) mimics typical potential terms used in molecular dynamics (MD) simulations except that the chi-square term. However our approach is not really MD simulations in that the weighting factor of the chi-square potential (c_2) in Eq. (7) is randomly generated for each structure within some limited range whose size depends on the number of simulation steps. In addition, to mimic the effect of simulated annealing, the allowed range for c_2 is reduced as simulation proceeds while other weighting factors c_1 and c_3 are fixed. After the movement of rigid bodies, the target function value is re-calculated and compared with the previous target function value for the structure before the movement. If the target function value is decreased and chemical bonds are maintained, the updated structure is accepted. Otherwise, that is, if the target function value is increased or any chemical bond is broken, the updated structure is not accepted. Then, the weighting factor of chi-square potential is randomly regenerated within the range and this cycle is repeated.

By following the steps described above, we can reduce the time taken for optimization because the structures are modified along the steepest direction or along the three force fields in the potential energy surface defined by the target function and the structures giving larger target

function value than the previous one are not accepted during the simulation. However, since the rigid bodies are moved according to a certain potential rather than being randomly moved to search a larger conformational space, the structure may be trapped in local minima. This problem is mitigated by using hundreds of random structures generated via the MC simulation as explained above.

Three terms in Eq. (7) are expressed as follows:

$$U_{LJ} = \sum_{i=1}^{N}\sum_{j\neq i}^{N} 4\left(\frac{\sigma^{12}}{r_{ij}^{12}} - \frac{\sigma^{6}}{r_{ij}^{6}}\right) \tag{8}$$

$$\chi^2 = \sum_{q=1}^{N_q}\left(\frac{\Delta S_{\exp}(q) - c_s \Delta S_{cal}(q)}{\sigma_q}\right)^2 \tag{9}$$

$$U_{SS} = \sum_{i=1}^{2/N}\sum_{j=1\neq i}^{2/N}\left(r_{ij} - r_{i+\frac{N}{2},j+\frac{N}{2}}\right)^2 + \sum_{i=\frac{N}{2}+1}^{N}\sum_{j=\frac{N}{2}+1\neq i}^{N}\left(r_{ij} - r_{i-\frac{N}{2},j-\frac{N}{2}}\right)^2 \tag{10}$$

The force field is the gradient of the potential, and therefore the force acting on a particle is expressed as follows:

$$\begin{aligned}
&\mathbf{f}_i = -\nabla_i U \\
&= 24c_1\sum_{j\neq i}^{N}\left(2\frac{\sigma^{12}}{r_{ij}^{13}} - \frac{\sigma^{6}}{r_{ij}^{7}}\right)\frac{\mathbf{r}_{ij}}{r_{ij}} \\
&+2c_2c_s\sum_{q=1}^{N_q}\left(\frac{\Delta S_{\exp}(q) - c_s\Delta S_{cal}(q)}{\sigma_q^2}\right)\sum_{j\neq i}^{N} f_i^s(q) f_j^s(q)\left(\cos(qr_{ij}) - \frac{\sin(qr_{ij})}{qr_{ij}}\right)\frac{\mathbf{r}_{ij}}{r_{ij}^2} \\
&-2c_3\left(\sum_{j=1\neq i}^{2/N}\left(r_{ij} - r_{i+\frac{N}{2},j+\frac{N}{2}}\right)\frac{\mathbf{r}_{ij}}{r_{ij}}\left(i \le \frac{N}{2}\right), \sum_{j=\frac{N}{2}+1\neq i}^{N}\left(r_{ij} - r_{i-\frac{N}{2},j-\frac{N}{2}}\right)\frac{\mathbf{r}_{ij}}{r_{ij}}\left(\frac{N}{2} < i < N\right)\right)
\end{aligned} \tag{11}$$

where σ value is the interatomic distance that makes Lennard-Jones potential be zero. We used 1.28 Å for the N-C bond, 2 Å for the bond between the heme domain and the histidine, and 1.2 Å for the atoms between two rigid bodies as the σ value. σ_q is standard deviation of experimental data and the $\mathbf{r}_{ij}$ (= $\mathbf{r}_i - \mathbf{r}_j$) is the relative position vector between particle i and particle j. To calculate the chi-square potential and force field, we use the Debye formula with solvent-corrected form factor ($f_j^s(q)$). Although the hydration shell term is ignored in the formula, it is

often used because of its mathematical simplicity and relatively small contribution of the hydration shell to the total scattering intensity [5-8]. This is especially true for the difference scattering curve.

According to the Debye formula, the scattering intensity can be expressed as follows [9]:

$$S(q) = \sum_{i=1}^{N}\sum_{j=1}^{N} f_i^s(q) f_j^s(q) \frac{\sin(qr_{ij})}{qr_{ij}} \tag{12}$$

The solvent-corrected form factor ($f_j^s(q)$) is

$$f_j^s(q) = f_j(q) - \rho_s g_j(q) \tag{13}$$

where $f_j(q)$ is the form factor of the *j-th* atom and $g_j(q)$ is the form factor of the solvent displaced by the *j-th* atom [2,6].

Forces acting on atoms in the protein are determined according to the three force fields described above and the motion is determined by Newtonian equations. Because we use the rigid-body approach, forces acting on atoms within a rigid body are added and then the total force determines translational motion of the rigid body. Meanwhile, the center of mass (COM) of a rigid body and individual forces on atoms determine the torque so that the rigid body is rotated. The coordinate of the COMs of rigid bodies (**R**) and relative position ($\mathbf{r}_i'$) of atoms from the COM of a rigid body that contains the atoms are calculated as follows:

$$\mathbf{R} = \frac{\sum m_i \mathbf{r}_i}{M} \tag{14}$$

$$\mathbf{r}_i' = \mathbf{r}_i - \mathbf{R} \tag{15}$$

where m_i is the mass of *i*th atom, and r_i is the coordinate of *i*th atom, and M is the mass of a rigid body ($M = \sum_i m_i$).

To calculate translational motion of a rigid body, the COM is updated according to the total force (**F**). The total force (**F**) is $\mathbf{F} = \sum_i \mathbf{f}_i$, and acceleration ($\ddot{\mathbf{R}}$) is determined as follows.

$$\ddot{\mathbf{R}} = \frac{\mathbf{F}}{M} \tag{16}$$

Meanwhile, rotational motion of a rigid body can be determined by calculating the total torque and the moment of inertia of a rigid body. When the COM is the center of rotation, the total torque (**N**) is:

$$\mathbf{N} = \sum_i \mathbf{r}_i^{'} \times \mathbf{f}_i \tag{17}$$

The moment of inertia is expressed as:

$$\mathbf{I} = \begin{bmatrix} \sum m_i(y_i^{'2} + z_i^{'2}) & -\sum m_i x_i^{'2} y_i^{'2} & -\sum m_i x_i^{'2} z_i^{'2} \\ -\sum m_i x_i^{'2} y_i^{'2} & \sum m_i(x_i^{'2} + z_i^{'2}) & -\sum m_i y_i^{'2} z_i^{'2} \\ -\sum m_i x_i^{'2} z_i^{'2} & -\sum m_i y_i^{'2} z_i^{'2} & \sum m_i(x_i^{'2} + y_i^{'2}) \end{bmatrix} \tag{18}$$

where $\mathbf{r}_i^{'} = (x_i^{'}, y_i^{'}, z_i^{'})$.

Then, the angular acceleration ($\dot{\boldsymbol{\omega}}$) is expressed as [10]:

$$\dot{\boldsymbol{\omega}} = \mathbf{I}^{-1} \cdot (\mathbf{N} - \boldsymbol{\omega} \times (\mathbf{I} \cdot \boldsymbol{\omega})) \tag{19}$$

The velocity of $\mathbf{r}_i^{'}$ relative to **R** is:

$$\dot{\mathbf{r}}_i^{'} = \boldsymbol{\omega} \times \mathbf{r}_i^{'} \tag{20}$$

In summary, the position of COM is updated from the translational motion and the relative positions ($\mathbf{r}_i^{'}$) of atoms within a rigid body are updated by the rotational motion. Finally, the coordinates of atoms ($\mathbf{r}_i$) are updated.

(6) Constraint to maintain the coordination

In HbI, the proximal histidine (His101) is bound to the heme via a coordination bond. To maintain the distance between the heme iron atom and His101, the two rigid bodies containing the iron and His101 are forced to move toward each other if the bond is elongated. The migration lengths of the two rigid bodies are determined so that the bond length is maintained at the equilibrium distance. The magnitude of movement of each rigid body was designed to be inversely proportional to the inner product value between the force vector acting on them and the direction vector of the coordination bond.

(7) Description of loop movement

In the rigid-body modeling, forces acting on two adjacent rigid bodies may differ in their directions and magnitudes, and the bond connecting the two rigid bodies might be elongated and be even broken. Some potential term preventing this extreme behavior can be applied, but it will limit the movement of rigid bodies. To solve this dilemma and describe the motion of loops more realistically while maintaining the integrity of bonds, the positions and shapes of the loops are repeatedly adjusted during the simulation instead of using any specific potential for the loops. Overall, three steps are performed for this purpose (see Figure S10).

In the first step, amino acids that constitute a loop are moved according to the relative movement of adjacent helices. In other words, the amino acids of the loop are moved gradually toward the next helix. However, by this step of movement, it is possible that specific bonds are more elongated than others. This elongation problem is resolved by rearranging positions of amino acids in the second step. The positions of amino acids in the loops are readjusted to make the C_α distances similar. So far only parallel translation of amino acids has been considered. In the final step, orientations of amino acids are adjusted to minimize the peptide bond lengths using C_α atoms as pivots. Especially, for the four terminus regions (N-terminus and C-terminus per one subunit), which may have relatively large movements due to their flexibilities, we performed an additional step to avoid elongation of bonds in loops that hold the terminus regions. If any bond connecting the terminus rigid body to the rest of the protein is elongated, we draw back the elongated terminus region to maintain the equilibrium bond length.

It turns out that these multiple steps of loop movement work effectively in the simulation of HbI probably because of its high helix content (~80%). Once the positions of the helices are determined, loops are repositioned to prevent bond breaking if any bond is to be broken. Actually, the loop correction may raise the target function value, but due to relatively higher content of helices than the loops, it turned out that the target function value gradually decreases during the simulation.

(8) Checking the mother structures

The mother structures, which are the original random structures before performing the chi-square minimization, of the candidate structures were traced back to check the structural space spanned by them. As shown in Figure S11, the mother structures of the 76 candidate structures for the I_3 intermediate show substantial structural variations and accordingly the distribution of their scattering curves are also widely scattered. This result confirms that the structure refinement used in our analysis works efficiently.

(9) Dependence on the choice of the HbI(CO)$_2$ structure

In the result of the structure refinement shown in Figure 4 of the main text, the structure of HbI(CO)$_2$ structure was fixed to be the 3sdh crystal structure. To check the dependence of the final refinement result on the choice of the HbI(CO)$_2$ structure, another structure (PDB code: 1nwn [11]) that has a RMSD of 0.3 Å with respect to 3sdh was also used. As shown in Figure S12, the results do not show significant dependence on the HbI(CO)$_2$ structure.

(10) Clustering method

The clustering method [12] was employed to select the representative structure. The method is usually used for analyzing the MD trajectory to extract common structural feature during the simulation time. We applied the method to find out structural similarity among the refined structures with minimized χ^2 values by the structure refinement. First, the root-mean-squares-deviations (RMSD) of C_α atoms of all possible pairs are calculated. Then, we count the number of neighbors using a certain cut-off value (0.4 Å) for all structures. Among the refined structures used in the clustering method, the structure that has the largest number of neighbors is considered as the first cluster. This process is repeated until all of the structures are clustered to several representative structures. Among the first-cluster structures, the structure that has a middle RMSD was selected as the representative structure and is proposed as the intermediate structure of the HbI photocycle.

(11) Example of structure refinement for I_3 (WT) intermediate

As described above, in order to extract the detailed structural changes such as helix movement and subunit rotation, we performed the structure refinement aided by Monte Carlo simulations for time-independent, species-associated scattering curves of the three intermediates. Each subunit of a HbI intermediate was divided into nine rigid bodies (eight helices and one heme group), giving a total of eighteen rigid bodies in the entire HbI protein. Starting from a crystal structure, Monte Carlo simulation was employed to generate many random structures by moving the rigid bodies. The result for the I_3 (WT) intermediate is shown as an example in Figure 4 in the main text. For each intermediate, 360 random structures were generated. For each of the initial random structures, we refined the structure by minimizing the degree of discrepancy (that is, χ^2 value) between the experimental curve and the theoretical curve calculated from the structure. To do so, we explored the structural space using Monte Carlo simulations guided by MD force fields and simulated annealing. In Figure 4A, the χ^2 values are plotted for the initial (black circles) and refined structures (red and blue circles) as a function of the root-mean-squares-deviation (RMSD) with respect to an arbitrary reference structure (deoxy-HbI, PDB code: 4sdh in this case). The wide range of the structural space consisting of these random structures is evident in the displacement plots of 50 random structures shown in Figure 4B. A displacement plot of a structure shows the displacement of amino acid residues compared with a reference structure as a function of the amino acid sequence and thus displays the tertiary structural difference between a structure of interest and a reference structure. Here the position of a residue is defined by the distance between Cα atom in the residue and the iron atom of the heme, and the displacement of the residue is the change in the distance between the two compared structures. As expected from the variety and high χ^2 values of the initial random structures, theoretical scattering curves calculated from those structures show a wide range of variations and do not match at all with the species-associated curve obtained from the experiment (Figure 4D).

Among 106 refined structures that have substantially reduced χ^2 values, we selected the representative structures by applying the clustering method. In the clustering method, the structures were categorized according to their structural similarities by comparing the RMSD values. As a result, 76 structures (out of 106) were classified as the first cluster and proposed as

the candidate structures (blue circles). A structure that has average RMSD among the first cluster was selected as a representative structure for the wild-type I_3 intermediate. The convergence to the optimized structure is confirmed by inspecting the displacement plots for all of the 76 candidate structures included in the first cluster. As shown in Figure 4C, the displacement plots for the candidate structures are well matched with each other. Naturally, the theoretical scattering curves from the best structures converge to the experimental species-associated scattering curve as shown in Figure 4E.

(12) Calculating the scaling factor between experimental and theoretical difference scattering curves

We calculated the scaling factor between the experimental species-associated difference scattering curves and theoretical difference scattering curves calculated in the middle of the structure refinement by using the laser-off scattering images, the static scattering curve of a capillary filled with buffer, and the theoretical scattering curve of the crystal structure of $HbI(CO)_2$ (3sdh). First, the scattering curves of laser-off images and the static scattering curves of a capillary with buffer were normalized by using the current values of storage ring and were averaged. We subtracted the averaged scattering curve of capillary with buffer from the averaged scattering curve of laser-off images and calculated the scaling factor by comparing with the theoretical scattering curve of $HbI(CO)_2$ calculated by CRYSOL. Because the difference scattering curves at all time delays were normalized in the range containing the isosbestic point of the water scattering curves with respect to temperature increase, the scattering curves of laser-off images were normalized in the same normalization range. The correction factor for different normalization standards was calculated and multiplied to the scaling factor. On the other hand, we found that the number of laser photons was much more than that of protein molecules in the focal volume of the X-ray. The number of photons and protein molecules within a unit volume at a certain position were calculated by considering that the laser power density, the sample concentration and the extinction coefficient at 532 nm (14.1 $mM^{-1}cm^{-1}$), then weighted according to the X-ray profile (0.09 mm x 0.06 mm centered at 0.1 mm below the surface of a capillary) assumed as a Gaussian function shape for each dimension. From the calculation, it turned out

that the condition regarding the power density of the laser was enough to excite all the protein molecules.

(13) Comparison of Data Measured at APS and KEK

As described above, the measurements were made in both 14IDB beamline at the APS and NW14A beamline at KEK. The heat-free time-resolved X-ray scattering data in the entire time range are shown in Figure S3 and Figure S13. Two representative time delays (10 ns and 31.6 μs) from the KEK and APS are compared in Figure S14. Since the energy spectra of the X-ray in the two beamlines are different, polychromatic correction was applied to compensate for different polychromatic effect. Scattering curves from APS and KEK are identical within the experimental error. The same kinetic analysis described above was applied to extract the kinetic parameters from the data from both APS and KEK. The results are presented and summarized in Figure S5 and Figure S7 for APS data and Figure S15 and Figure S16 for KEK data. It can be seen that the same kinetic model was used for the APS data and the obtained kinetic parameters are identical. Those results indicate that our measurements are highly reproducible and independent of the facility.

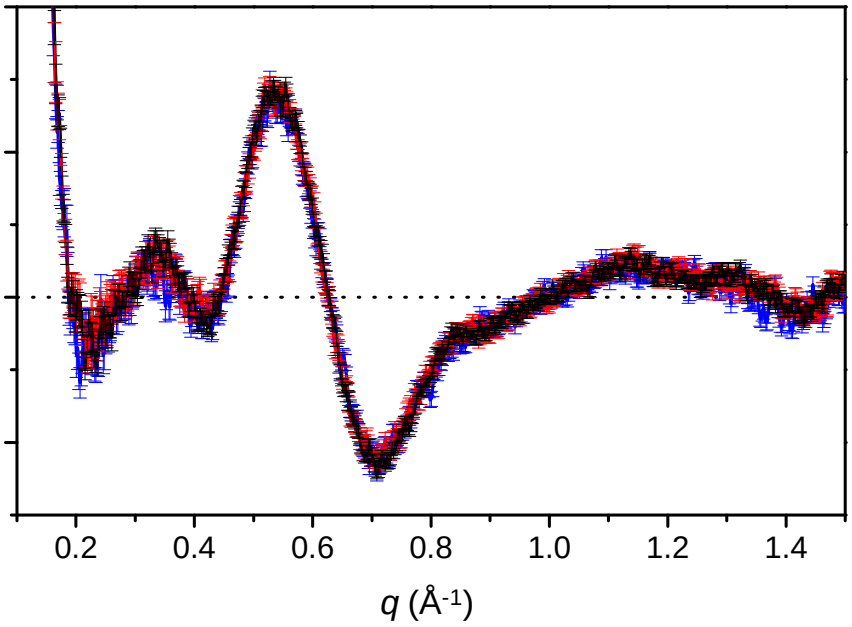

Figure S1. The 31.6 μs data measured from three different data collection schemes listed in Table S2 are compared. The three curves are basically identical within the experimental error.

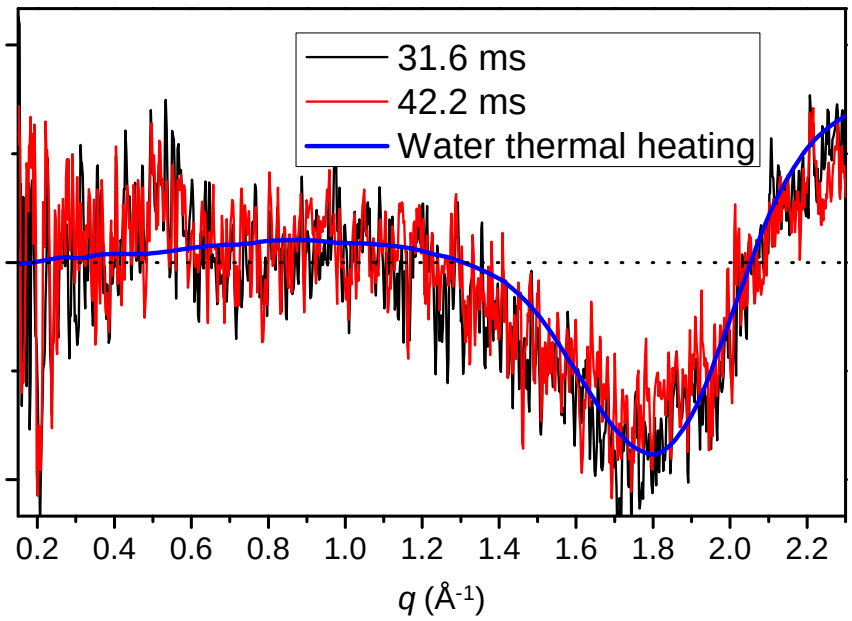

Figure S2. The scattering data at 31.6 ms (black) and 42.2 ms (red) time delays. At these time delays, the signal at low q values (< 1.0 $Å^{-1}$) is absent, indicating that the contribution from transiently generated species is negligible. Difference curves at 31.6 ms and 42.2 ms can be represented by a sum of contributions from thermal heating of bulk water (blue), that is, the temperature change at constant density ($(\partial S(q)/\partial T)_\rho$) and the density change at constant temperature ($(\partial S(q)/\partial \rho)_T$). This observation confirms that the difference signals at late time delays are mainly attributed to solvent heating.

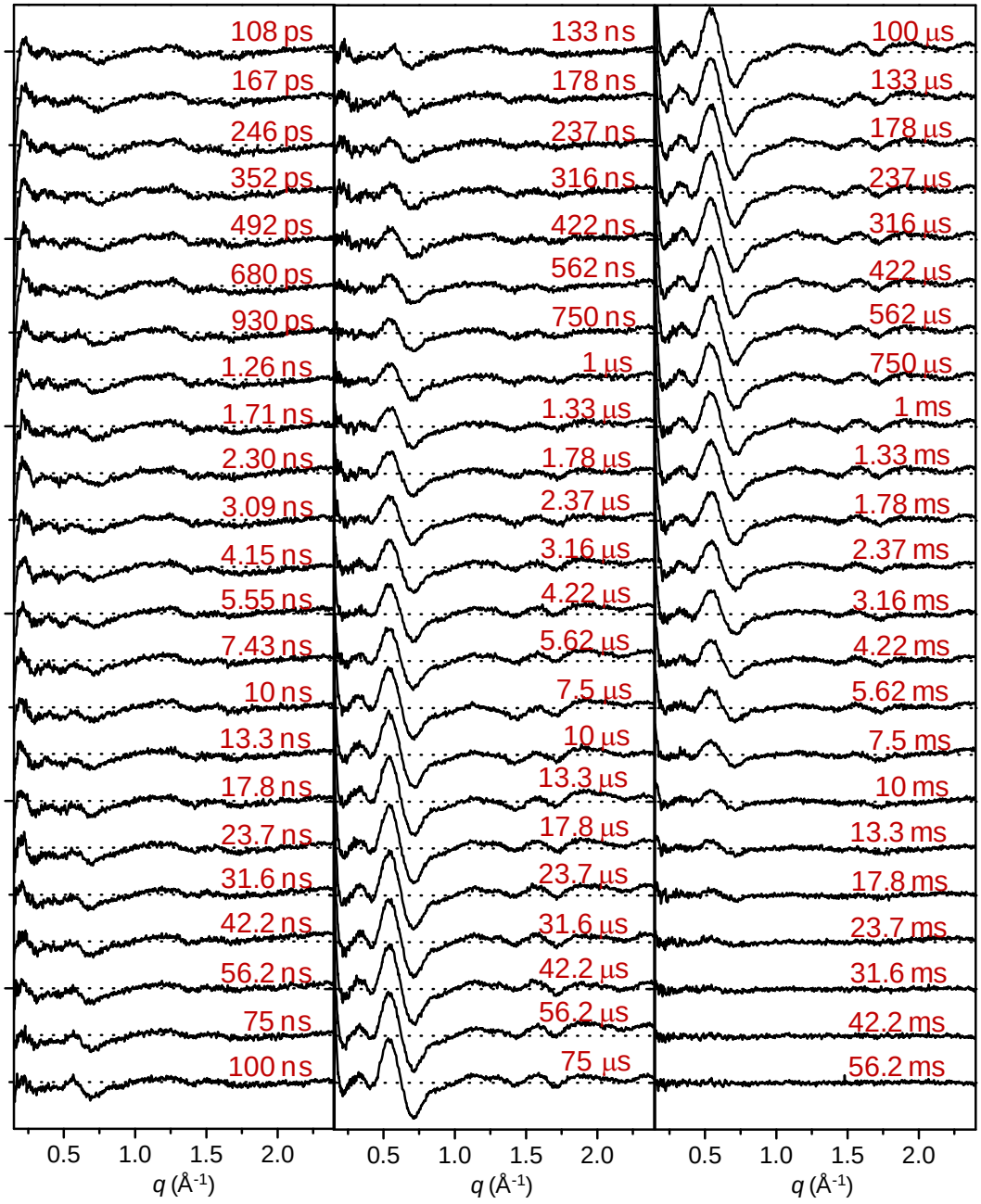

Figure S3. Heat-free, time-resolved X-ray scattering data of the wild-type HbI (measured at APS). Thermal heating signal of bulk water shown in Figure S2 was subtracted from the original difference curves.

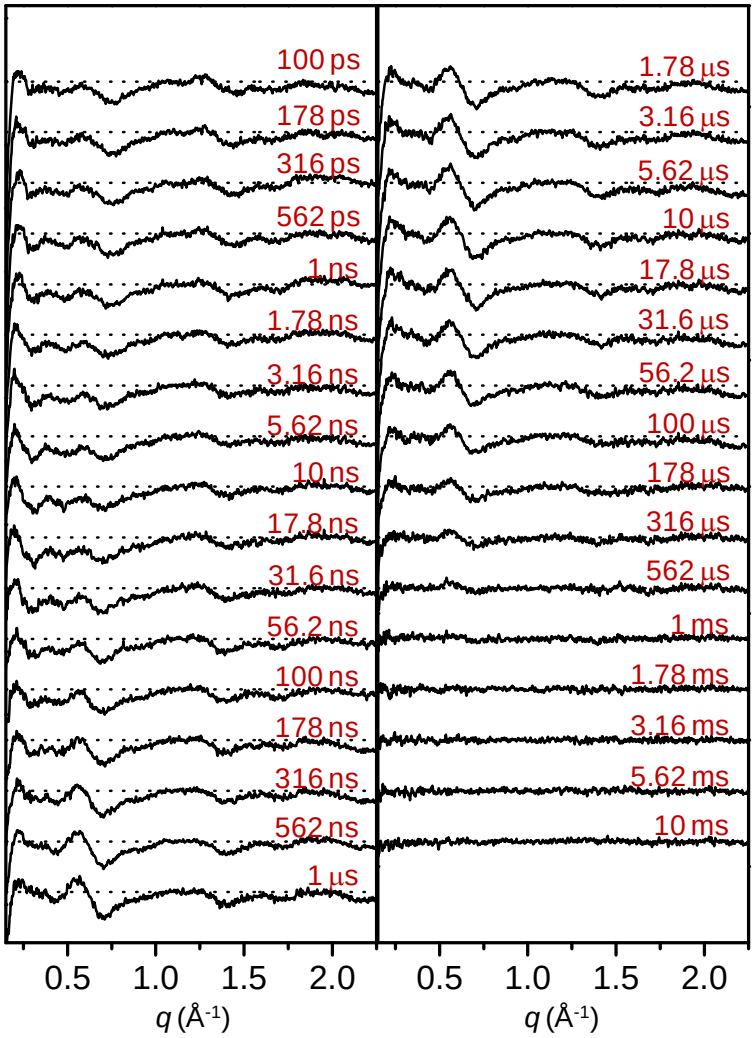

Figure S4. Heat-free, time-resolved X-ray scattering data of the F97Y mutant (measured at APS). Thermal heating signal of bulk water was subtracted from the original difference curves.

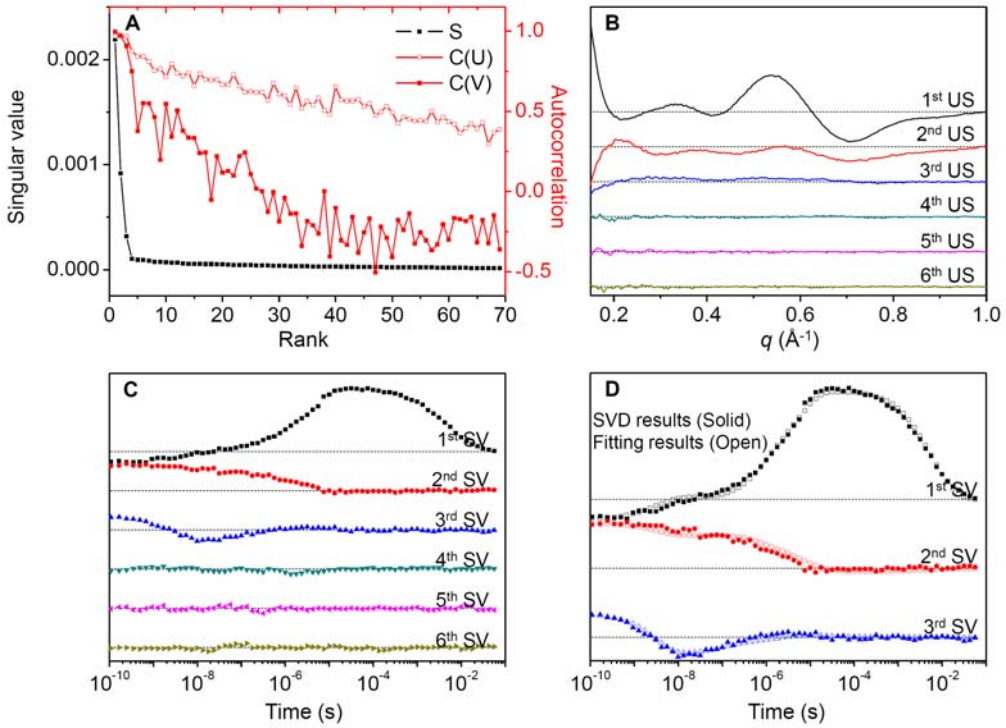

Figure S5. (A) Singular values (black solid square), autocorrelations of left singular vectors (*U*, red open square) and right singular vectors (*V*, red solid square) obtained from time-resolved difference X-ray solution scattering data measured at APS are shown for wild-type HbI excited with 'mid' laser fluence. Judging by the amplitude of the singular values and the autocorrelations, we employed the first three (both left and right) singular vectors for our kinetic analysis. (B) The first six left singular vectors multiplied by singular values are shown. (C) The first six right singular vectors multiplied by singular values are shown. Among these, the first three right singular vectors multiplied by singular values were fit by seven exponentials sharing common time constants, yielding the time constants of 3.2 (± 0.2) ns, 93 (± 20) ns, 730 (± 120) ns, 5.6 (± 0.8) µs, 15.2 (± 8) µs, 1.8 (± 0.3) ms, and 9.1 (± 0.9) ms. (D) By kinetic analysis, the first three right singular vectors multiplied by singular values were fit using a linear combination of "I_1", "I_2", and "I_3" populations calculated from the kinetic model. Through this fitting procedure, we obtained the coefficient matrix that is used to calculate species-associated difference scattering curves.

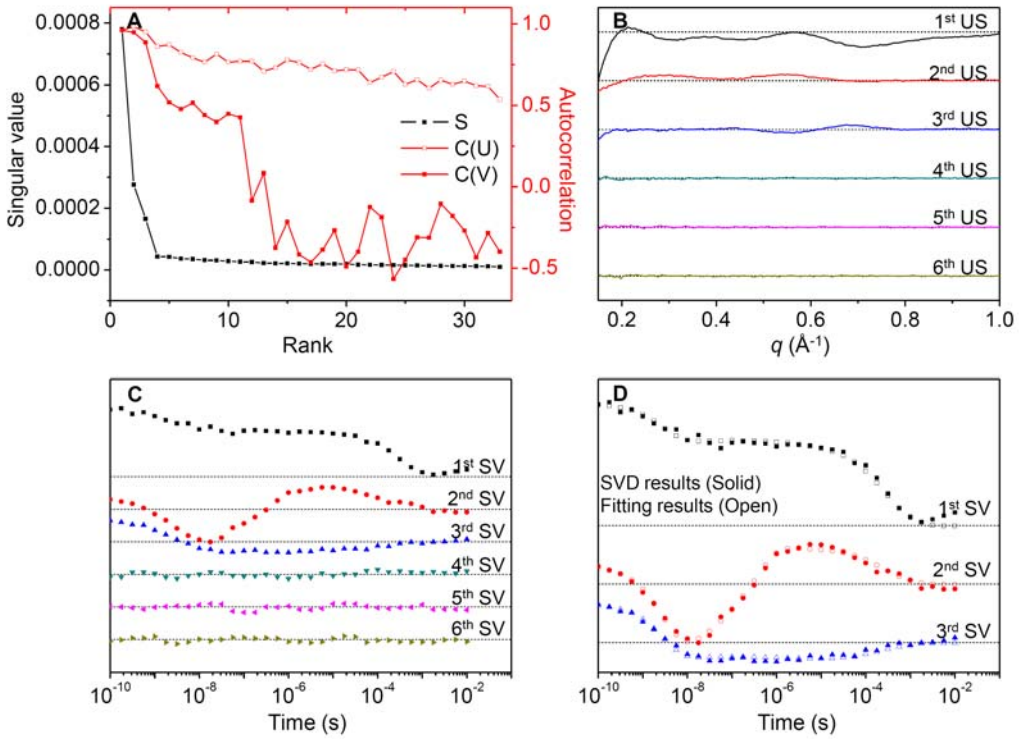

Figure S6. The same analysis as in Figure S5, but for F97Y mutant. (A) Singular values (black solid square), autocorrelations of left singular vectors (*U*, red open square) and right singular vectors (*V*, red solid square) obtained from time-resolved difference X-ray solution scattering data measured at APS are shown for F97Y mutant HbI excited with 'mid' laser fluence. As for wild-type HbI, we employed the first three (both left and right) singular vectors for our kinetic analysis. (B) The first six left singular vectors multiplied by singular values are shown. (C) The first six right singular vectors multiplied by singular values are shown. The first three right singular vectors multiplied by singular values were fit by using six exponentials sharing common time constants, yielding the time constants of 3.0 (± 0.3) ns, 40 (± 20) ns, 370 (± 100) ns, 4.7 (± 3.1) µs, 25.9 (± 13.8) µs, and 330 (± 40) µs were obtained. (D) By kinetic analysis, the first three right singular vectors multiplied by singular values were fit using a linear combination of "I_1", "I_2", and "I_3" populations calculated from the kinetic model. Through this fitting procedure, we obtained the coefficient matrix that is used to calculate species-associated difference scattering curves.

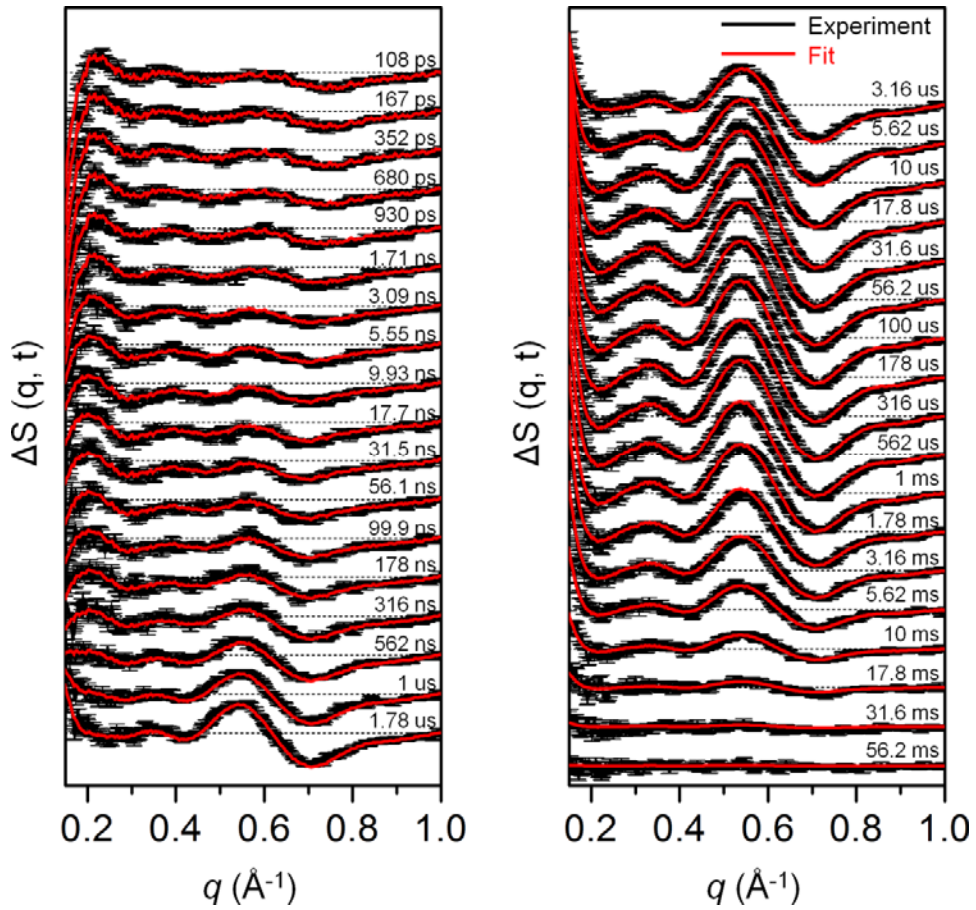

Figure S7. Time-resolved difference X-ray solution scattering data, $\Delta S(q,t)$, of the wild-type HbI excited with 'mid' laser fluence (measured at APS). Experimental curves (black) are compared with theoretical curves (red) that were generated from linear combinations of three time-independent species-associated scattering curves extracted from the kinetic analysis.

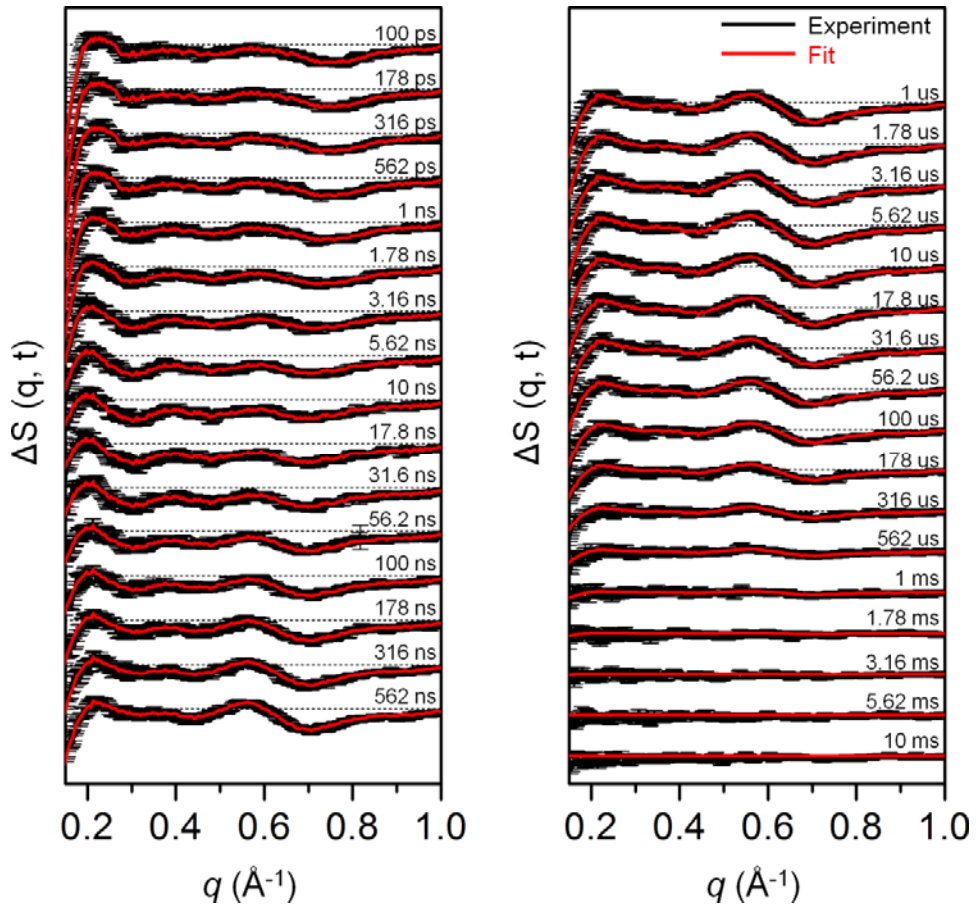

Figure S8. Time-resolved difference X-ray solution scattering data, $\Delta S(q,t)$, of the F97Y mutant excited with 'mid' laser fluence (measured at APS). Experimental curves (black) are compared with theoretical curves (red) that were generated from linear combinations of three time-independent species-associated scattering curves extracted from the kinetic analysis.

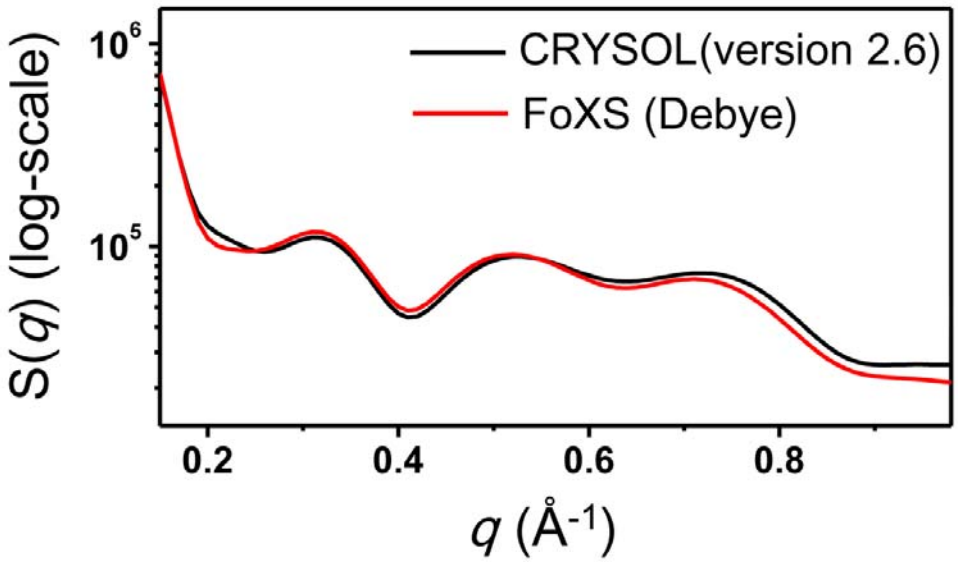

Figure S9. Comparison of the scattering curves calculated by using CRYSOL (version 2.6) and FoXS for a PDB file (4sdh).

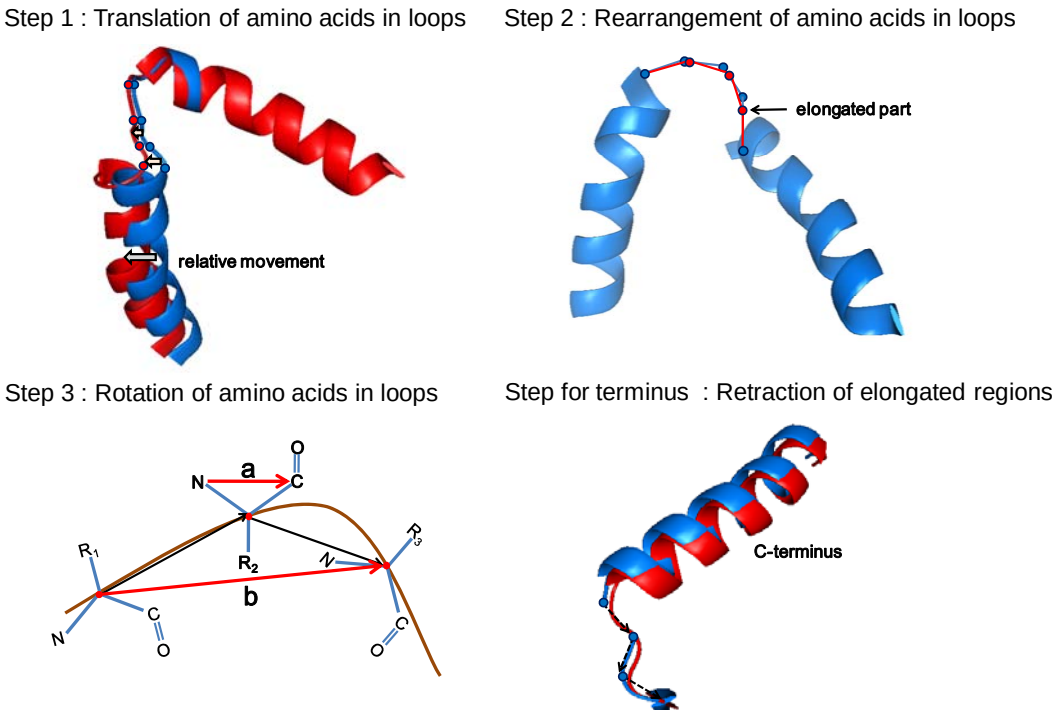

Figure S10. The step-by-step procedure for loop adjustment in the rigid-body modeling.

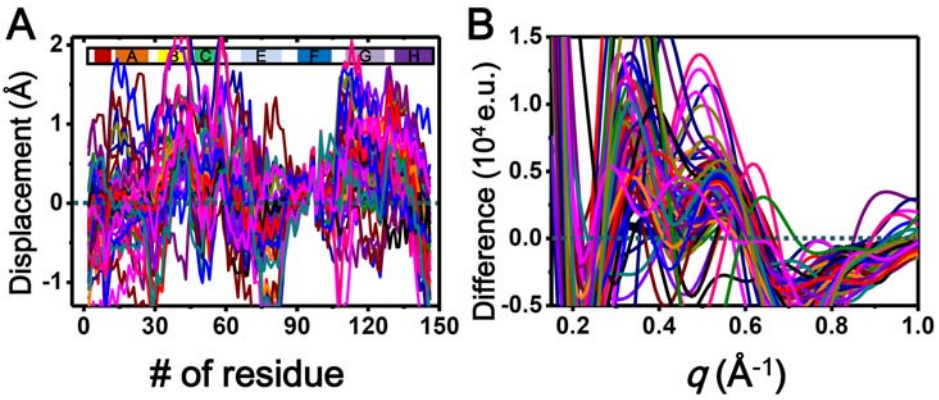

Figure S11. (A) The displacement plots for the mother structures of the candidate structures for the I_3 (WT) intermediate. (B) The difference scattering curves calculated from the mother structures.

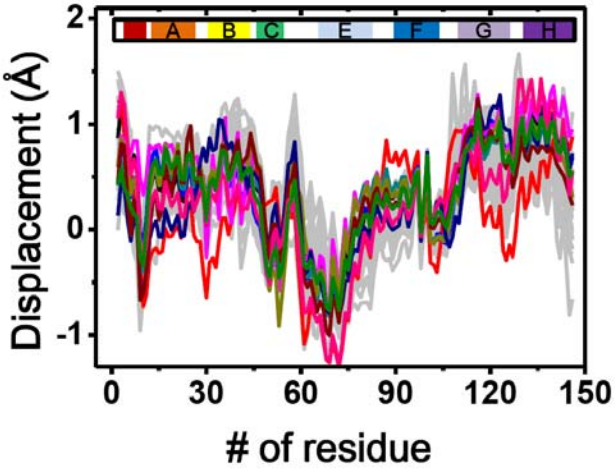

Figure S12. Dependence of the result from the structure refinement (represented as displacement plots) on the choice of the $HbI(CO)_2$ structure. The gray curves are superimposed displacement plots of the refined candidate structures of the I_3 (WT) intermediate when the 3sdh structure was used for the $HbI(CO)_2$ structure. The other colored curves are displacement plots obtained when another $HbI(CO)_2$ structure (1nwn) was used for the $HbI(CO)_2$ structure. The overall patterns converge regardless of the choice of the $HbI(CO)_2$ structure.

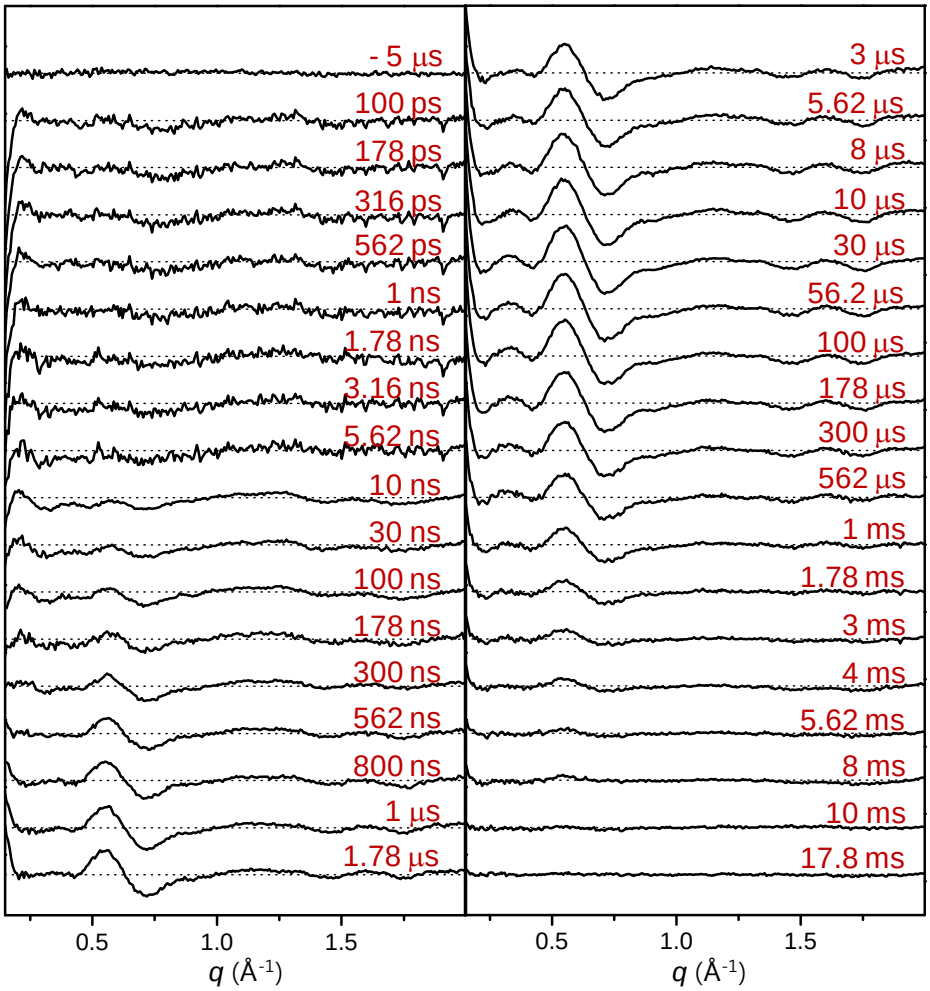

Figure S13. Heat-free, time-resolved X-ray scattering data measured at KEK. Thermal heating signal of bulk water was subtracted from the original difference curves.

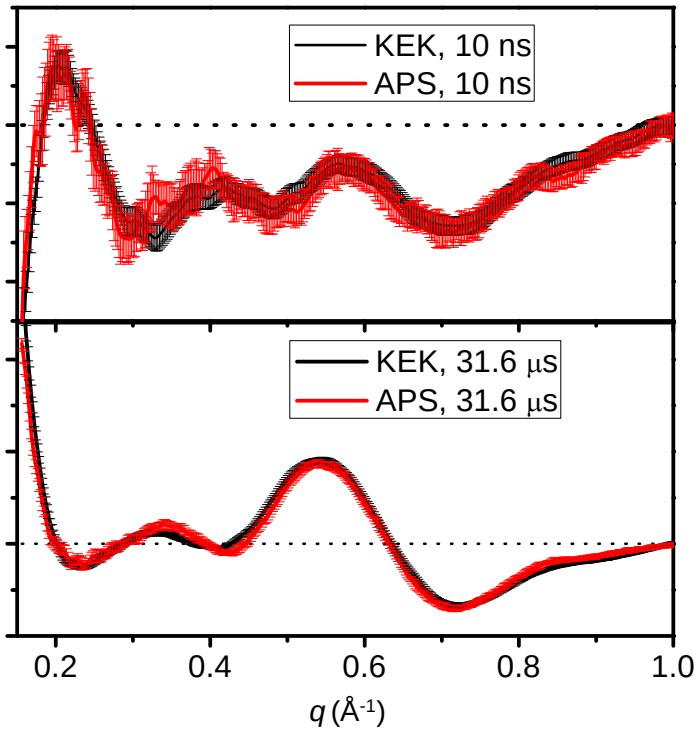

Figure S14. Difference scattering curves of the HbI protein at 10 ns (top) and 31.6 μs (bottom) time delays measured at KEK (black) and APS (red). The data from the two different beamlines at each representative time delay are identical within the experimental error. Since the energy spectra of the polychromatic X-ray beam in the two beamlines are different, polychromatic correction was applied to compensate for the polychromatic effect.

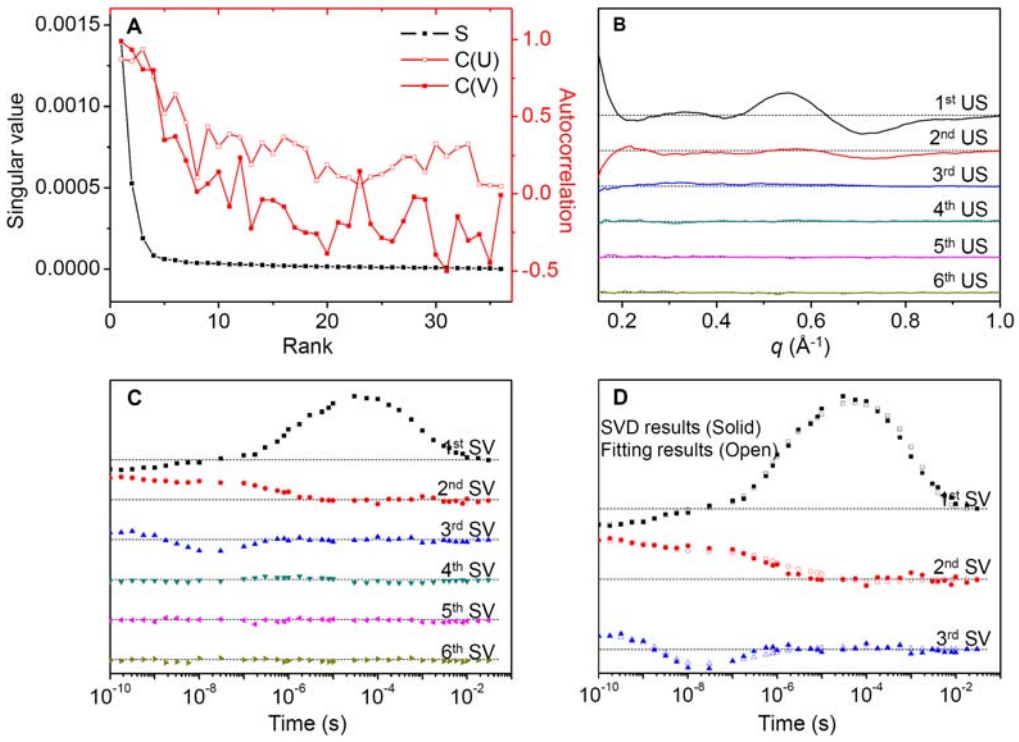

Figure S15. The same analysis as in Figure S5, but for the data of the wild type measured at KEK. (A) Singular values (black solid square), autocorrelations of left singular vectors (*U*, red open square) and right singular vectors (*V*, red solid square) obtained from time-resolved difference X-ray solution scattering data measured at KEK are shown for the wild-type HbI excited with 'high' laser fluence. Judging by the amplitude of the singular values and the autocorrelations, we employed the first three (both left and right) singular vectors for our kinetic analysis. (B) The first six left singular vectors multiplied by singular values are shown. (C) The first six right singular vectors multiplied by singular values are shown. The first three right singular vectors multiplied by singular values were fit by using seven exponentials sharing common time constants, yielding the time constants of 3.4 (± 0.5) ns, 170 (± 80) ns, 770 (± 160) ns, 8.7 (± 2.7) µs, 34.6 (± 27.2) µs, 580 (± 110) µs, and 4.0 (± 0.8) ms. (D) By kinetic analysis, the first three right singular vectors multiplied by singular values were fit by a linear combination of "I_1", "I_2", and "I_3" populations calculated from the kinetic model. Through this fitting procedure, we obtain the coefficient matrix that is used to calculate species-associated difference scattering curves.

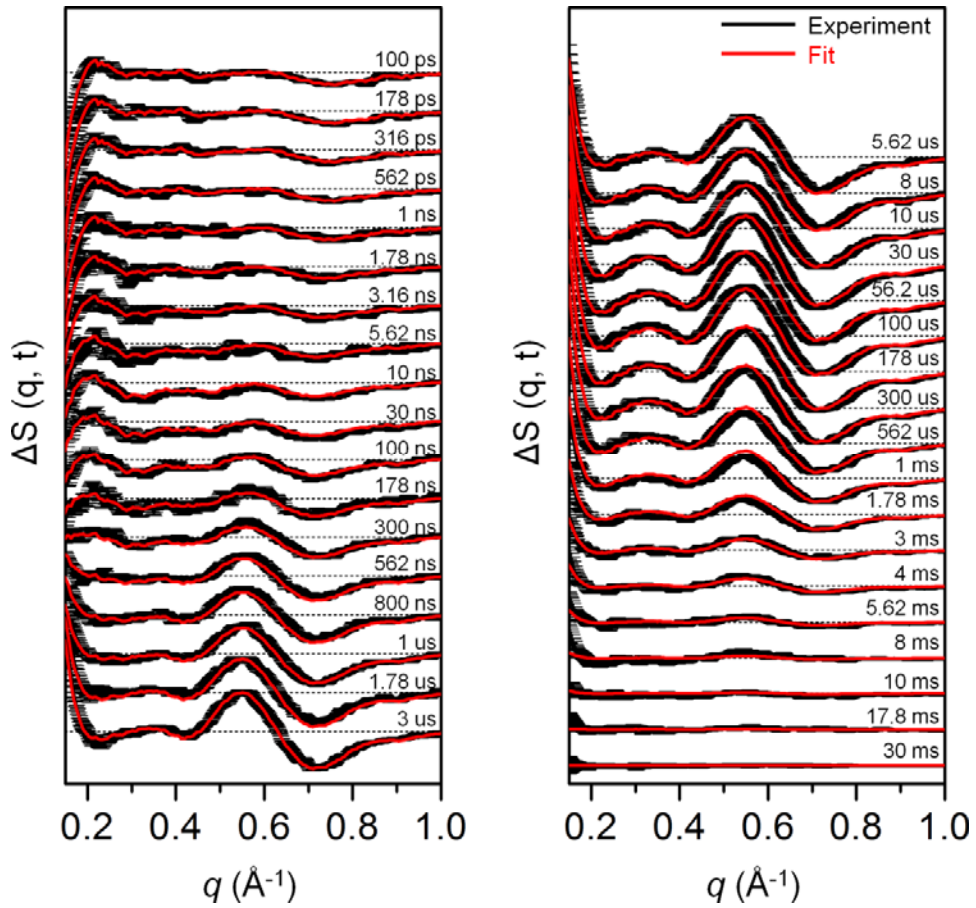

Figure S16. Time-resolved difference X-ray solution scattering data, $\Delta S(q,t)$, of the wild-type HbI excited with 'high' laser fluence (measured at KEK). Experimental curves (black) are compared with theoretical curves (red) that were generated from linear combinations of three time-independent species-associated scattering curves extracted from the kinetic analysis.

Table S1. Summary of beamtimes used for the data collection.

Date	Beamline	Time range	Laser fluence (mJ/mm^2)
2009. 3	KEK	30 μs - 56.2 ms	2.0
2009. 6	KEK	10 ns – 56.2 ms	2.0
2009. 12	KEK	10 ns – 56.2 ms	2.0
2010. 2	KEK	10 ns – 56.2 ms	0.5, 1, 2.0
2010. 5	KEK	10 ns – 56.2 ms	2.0, 2.5
2010. 10	KEK	100 ps – 10 ns 30 μs – 56.2 ms	0.5
2010. 11	APS	100 ps – 56.2 ms	0.25, 0.5, 1
2011. 7	APS	100 ps – 10 ms	0.5

Table S2. Details of the data-collection parameters.

	1st scheme	**2nd scheme**	**3rd scheme**
Time delays	–5 μs, 108 ps, 167 ps, 246 ps, 352 ps, 492 ps, 680 ps, 930 ps, 1.26 ns, 1.71 ns, 2.30 ns, 3.09 ns, 4.15 ns, 5.55 ns, 7.43 ns, 10 ns, 13.3 ns, 17.8 ns, 23.7 ns, 31.6 ns, 42.2 ns, 56.2 ns, 75 ns, 100ns, 133 ns, 178 ns, 237 ns, 316 ns, 422 ns, 562 ns, 31.6 μs	–5 μs, 562 ns, 750 ns, 1 μs, 1.33 μs, 1.78 μs, 2.37 μs, 3.16 μs, 4.22 μs, 5.62 μs, 31.6 μs	–5 μs, 5.62 μs, 7.5 μs, 10 μs, 13.3 μs, 17.8 μs, 23.7 μs, 31.6 μs, 42.2 μs, 56.2 μs, 75 μs, 100 μs, 133 μs, 178 μs, 237 μs, 316 μs, 422 μs, 562 μs, 750 μs, 1 ms, 1.33 ms, 1.78 ms, 2.37 ms, 3.16 ms, 4.22 ms, 5.62 ms, 7.5 ms, 10 ms, 13.3 ms, 17.8 ms, 23.7 ms, 31.6 ms, 42.2 ms, 56.2 ms
X-ray pulses per chopper opening	1	Multi bunch	Multi bunch
Pump-probe pulse pairs per image	1100	1100	100
X-ray pulse duration	100 ps	~250 ns	~1.5 μs
Laser pulse width	30 ps	30 ps	30 ps
Laser fluence	0.25 mJ/mm^2, 0.5 mJ/mm^2, 1.0 mJ/mm^2		

Table S3. Definitions for parameters in the kinetic model.

Parameter	Description
D	Bimolecular rebinding rate of I_3 (singly liganded species)
Matrix **P**	3 x 3 coefficient matrix to calculate species-associated difference scattering curves
g	Relative ratio of the geminately recombined species
f	Relative ratio of the fully photolyzed species
C_0	Equilibrium CO concentration
[HbI]	Sample concentration

Table S4. Fitting parameters obtained from the kinetic analysis of the TR-WAXS data of HbI measured at APS.

Parameter	**Best fit value**				**Error**			
	Wild-type HbI			**F97Y**	**Wild-type HbI**			**F97Y**
D	95 $mM^{-1}s^{-1}$			1310 $mM^{-1}s^{-1}$	1 $mM^{-1}s^{-1}$			20 $mM^{-1}s^{-1}$
	min	**mid**	**high**	**mid**	**min**	**mid**	**high**	**mid**
g	28.6 %	23.5 %	19.3 %	1.9 %	0.3 %	0.2 %	0.3 %	0.1 %
f	37.0 %	40.2 %	54.5 %	18.5 %	0.6 %	0.3 %	0.2 %	0.3 %
C_0	0.93 mM			0.93 mM	--			--
[HbI]	2.0 mM			3.5 mM	--			--

The double dash "--" indicates that the parameter was fixed during the fitting procedure. Values reported in the "Error" column correspond to ± one standard deviation.

Table S5. Fitting parameters resulting from the kinetic analysis in terms of the allosteric kinetic model using KEK wild-type HbI data

Parameter	Best fit value	Error
D	340 $mM^{-1}s^{-1}$	1.7 $mM^{-1}s^{-1}$
	higher than 1.0 mJ/mm^2 (high)	**higher than 1.0 mJ/mm^2 (high)**
g	17.9 %	0.50 %
f	64.6 %	0.29 %
C_0	0.93 mM	--
[HbI]	2.0 mM	--

The double dash "--" indicates that the parameter was fixed during the fitting procedure. Values reported in the "Error" column correspond to ± one standard deviation.

References

(1) Summerford, C. M.; Pardanani, A.; Betts, A. H.; Poteete, A. R.; Colotti, G.; Royer, W. E., Jr. *Protein Eng.* **1995**, *8*, 593.
(2) Svergun, D.; Barberato, C.; Koch, M. H. J. *J. Appl. Cryst.* **1995**, *28*, 768.
(3) Schneidman-Duhovny, D.; Hammel, M.; Sali, A. *Nucl. Acid Res.* **2010**, *38*, W540.
(4) Kojima, M.; Timchenko, A. A.; Higo, J.; Ito, K.; Kihara, H.; Takahashi, K. *J. Appl. Cryst.* **2004**, *37*, 103.
(5) Grishaev, A.; Wu, J.; Trewhella, J.; Bax, A. *J. Am. Chem. Soc.* **2005**, *127*, 16621.
(6) Tiede, D. M.; Zhang, R.; Seifert, S. *Biochemistry* **2002**, *41*, 6605.
(7) Zhang, R. T.; Thiyagarajan, P.; Tiede, D. M. *J. Appl. Cryst.* **2000**, *33*, 565.
(8) Chacon, P.; Moran, F.; Diaz, J. F.; Pantos, E.; Andreu, J. M. *Biophys. J.* **1998**, *74*, 2760.
(9) Guinier, A. *X-Ray Diffraction: In Crystals, Imperfect Crystals, and Amorphous Bodies*; Dover Publications: New York, 1994.
(10) Goldstein, H. *Classical Mechanics*; Addison-Wesley Publishing Company, Inc, 1980.
(11) Knapp, J. E.; Royer, W. E., Jr. *Biochemistry* **2003**, *42*, 4640.
(12) van Gunsteren, W. F.; Daura, X.; Gademann, K.; Jaun, B.; Seebach, D.; Mark, A. E. *Angew. Chem. Int. Ed.* **1999**, *38*, 236.